Mechanical metamaterials: nonlinear beams and excess zero modes

Lubbers, L.A.

3

Excess zero modes in metamaterials with symmetries

We study the excess zero modes that arise for randomly diluted collections of rigid quadrilaterals, linked by flexible hinges at their tips. For full filling (no quads removed), large systems built from generic quads are rigid. In contrast, large symmetric systems featuring regular, identical squares possess one zero mode [1, 20], irrespective of size. Here we reveal the surprising finding that the number of such excess zero modes can become larger than one in systems where quads are randomly removed, demonstrating the existence of excess zero modes beyond a global hinging mode. Specifically, we show that the average number of excess modes for a large ensemble of randomly diluted systems, $\langle \Delta \rangle$, exceeds one and displays a peak with the fraction of removed quads, ρ, which consistently grows with the system size N. Interestingly, $\langle \Delta \rangle (\rho, N)$ exhibits finite size scaling with simple mean field exponents, suggesting the number of excess modes is an intrinsic quantity, and we obtain similar results for random bond (hinge) removal. Finally, we study the distribution of excess zero modes near the peak and design extreme geometries whose density of zero modes is six times larger than the peak average.

A paper based on the work presented in this chapter is in preparation for submission to Phys. Rev. Lett. as:

L.A. Lubbers and M. van Hecke, *Excess floppy modes in metamaterials with symmetries.*

3.1 Introduction

Collections of stiff elements connected by flexible hinges form a basis model for a wide range of systems, including engineering structures, complex materials and mechanical metamaterials. Depending on the multitude and geometry of links between the elements, such structures can be either floppy or rigid. Here we introduce counting arguments, that, by comparing the number of degrees of freedom and the number of constraints, determine the rigidity of such systems. We start by introducing Maxwell counting, and then show that this simple approach is not sufficient to determine the number of zero modes, due to the potential presence of states of self-stress.

3.1.1 Maxwell counting

In 1864 Maxwell laid the foundation for determining the rigidity of frames [51]. He geometrically described a frame as a system consisting of sites (points) that are connected by bonds (lines). When the sites are connected by a sufficient amount of bonds, the frame becomes rigid and no site(s) can be displaced without stretching or compression of bonds. When the sites are connected by too few bonds, however, the structure features zero modes, which are zero energy deformations that do not stretch bonds. A simple estimate of the relation between the number of sites N_s, bonds N_b and zero modes n_{m} in d dimensions, is given by the Maxwell count, and

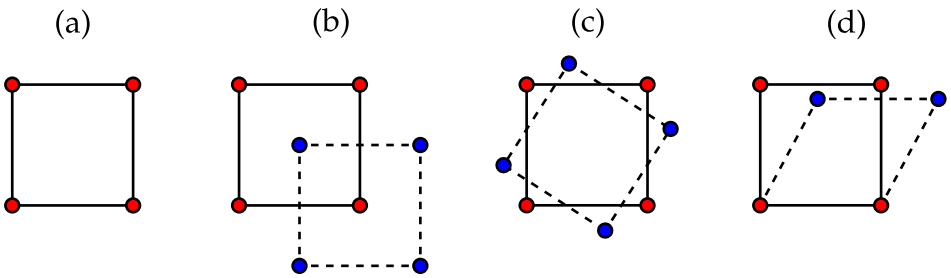

Figure 3.1: Sites, bonds and zero modes. (a) A square frame built from sites (filled circles) and bonds (black lines) has 4 zero modes ($n_m = 4$). (b-c) Trivial zero modes. Panel (b) shows global translation and panel (c) shows global rotation. (d) Internal zero mode.

reads

$$dN_s - N_b = n_m. \tag{3.1}$$

Here, the term dN_s represents the total number of degrees of freedom of the (unconnected) sites, tantamount to d independent translational degrees of freedom per site. The second term equals the number of constraints and is simply equal to N_b. Hence, the Maxwell count can physically be interpreted as a balance between the total number of degrees of freedom and constraints in the system, whose difference yields the number of zero modes.

We now exemplify the Maxwell count for the two-dimensional frame depicted in Fig. 3.1(a), which consists of $N_b = 4$ bonds and $N_s = 4$ sites. Applying Eq. (3.1) using $d = 2$ we find that the frame attains $n_m = 2 \times 4 - 4 = 4$ zero modes. Of these, three are trivial zero modes associated with global translations and rotations [Fig. 3.1(b-c)]. The remaining zero mode is shown in Fig. 3.1(d), and involves internal displacements of the sites. Hence, when focusing on internal zero modes, we exclude the $d(d+1)/2$ global zero modes, and rewrite the Maxwell criterium as

$$dN_s - N_b = n_m^i + \frac{d\,(d+1)}{2}, \tag{3.2}$$

where n_m^i are the internal zero modes. A frame is called stiff when $n_m^i = 0$. Internal zero modes that allow for finite-amplitude displacements of the sites are also called mechanisms, in contrast to infinitesmall zero modes where changes in the energy are at most quartic in the displacement amplitude.

We now present examples that show that Maxwell counting is not exact. To do so, we add diagonal bonds to the square frame, as shown in Fig. 3.2. First, for a single diagonal bond [panel (a)] the frame becomes stiff and we anticipate $n_m^i = 0$. Indeed, Eq. (3.2) confirms that $n_m^i = 2 \times 4 - 5 - 3 = 0$, and Maxwell's rule applies. For a second diagonal bond [panel (b)], we still anticipate $n_m^i = 0$, but the Maxwell count would predict $n_m^i = -1$. This inconsistency is caused by the second diagonal bond, which is redundant, and not needed for the rigidity of the square frame. Redundant bonds introduce so called states of self-stress in the system, which are combinations of tensions and compressions on the bonds that result in a zero net force on all sites. The combination of

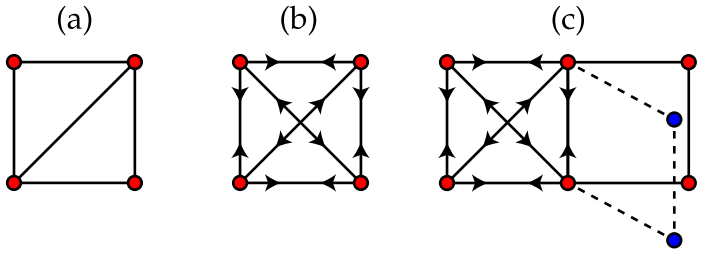

Figure 3.2: States of self-stress. (a) A square frame with a single diagonal bond is isostatic ($n_m^i = n_{ss} = 0$). (b) For two diagonal bonds, the square frame exhibits a single state of self-stress ($n_m^i = 0, n_{ss} = 1$), as indicated by the arrowheads. (c) Frame with one state of self-stress and one internal zero mode ($n_m^i = 1, n_{ss} = 1$).

such tensions and compressions that compose the (single) state of self-stress for the frame in panel (b), is visualized by the black arrows. In this state of self-stress, side bonds are placed under compression and diagonal bonds under tension. In order to accurately predict n_m^i for frames holding redundant bonds, or rather holding n_{ss} self-stresses, a modified criterium that takes into account these self-stresses is necessary. This modified criterium is known as the generalized Maxwell equation, and is given by

$$dN_s - N_b = n_m^i + \frac{d\,(d+1)}{2} - n_{ss}. \tag{3.3}$$

Note that Eq. (3.3) indeed predicts $n_m^i = 0$ for the frame in panel (b) for $n_{ss} = 1$. Frames that neither attain internal zero modes nor have any states of self-stress are called isostatic ($n_m^i = n_{ss} = 0$). Hence, a square frame with a single diagonal is isostatic, but a square frame with two diagonals is not. Finally, we illustrate the generalized Maxwell relation for a more complicated frame, which is shown in Fig. 3.2(c). This frame can be regarded as a combination of an over-constrained region (left square frame) and a floppy region (right square frame), and consequently has $n_m^i = 1$ and $n_{ss} = 1$. Based on the global number of sites and bonds, Eq. (3.3) predicts $n_m^i - n_{ss} = 0$, which demonstrates that the generalized Maxwell equation holds.

3.1.2 This chapter

In this chapter, we study systems that consist of quadrilaterals (quads) linked by flexible hinges at their tips. We will consider and compare generic systems, consisting of irregular quads, to symmetric systems, consisting of identical squares (regular quads). A special property of symmetric systems —which plays a central role in this chapter— is that these systems always feature a hinging zero mode, even for full filling (no squares removed), and independent of the system size. This is not necessarily true for generic systems, as we will demonstrate now by applying the generalized Maxwell count to $N_x \times N_y$ lattices of quads.

To set up the counting argument we need the following two ingredients. First, a single quad has 3 degrees of freedom, namely two translational and one rotational. Second, every hinge, or bond, is equivalent to two constraints. This is most easily understood by considering two separate quads: Their translational degrees of freedom couple when joining any pair of tips, effectively reducing the degrees of freedom by two. Taking these considerations into account, a system of $N_x \times N_y$ squares has a total of $3N_xN_y$ degrees of freedom and $N_x\left(N_y-1\right)+N_y\left(N_x-1\right)$ bonds, equivalent to $4N_xN_y-2\left(N_x+N_y\right)$ constraints. Adapting the generalized Maxwell count as given in Eq. (3.3) to the context of quads, we obtain

$$n_m^i - n_{ss} = -N_xN_y + 2\left(N_x+N_y\right) - 3, \tag{3.4}$$

where we note that the above equation holds for generic and symmetric systems. Now, if the balance $n_m^i - n_{ss}$ exceeds zero the system must have internal zero modes. If $n_m^i - n_{ss} \leq 0$, the system might attain zero modes, depending on the number of states of self-stress. Using N_y as the control parameter, we have evaluated Eq. (3.4) for several values of N_y and tabulated the results in Table 3.1. We now discuss the implications of

N_y	$n_m^i - n_{ss}$
1	$N_x - 1$
2	1
3	$3 - N_x$

Table 3.1: Eq. (3.4) evaluated for $N_y = 1,2,3$.

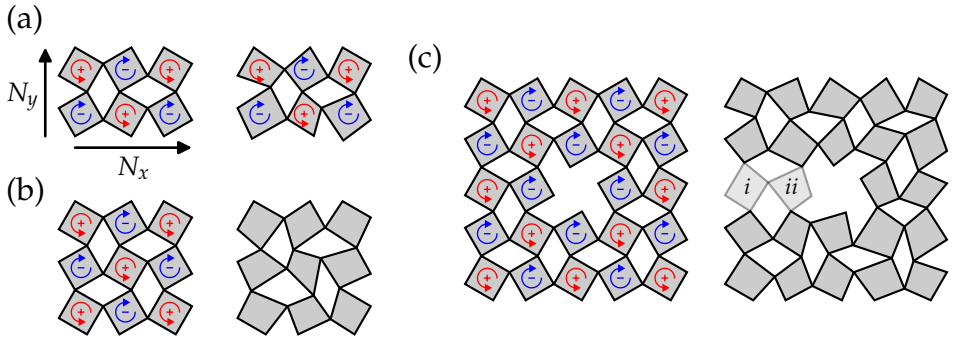

Figure 3.3: Rigidity of strips, 3×3 clusters and looped-strips. (a-c) In each panel, we compare symmetric (left) and generic (right) systems. The coloured arrows indicate a global hinging mode, in which quads collectively counter rotate. (a) Strips always attain a global hinging mode, both in the generic and symmetric case ($n_s = n_g = 1$). (b-c) In contrast, 3×3 clusters (b) or looped-strips (c) only attain a global hinging zero mode when the system is symmetric ($n_s = 1, n_g = 0$). Note that one recovers an ordinary strip ($n_s = n_g = 1$) by the removal of quads *i* and *ii* (illustrated by their lower opacity).

this table for the rigidity of the three basic geometries shown in Fig. 3.3, which will be encountered frequently throughout this chapter.

> In the remainder of this thesis, we make a clear distinction between n_m^i for symmetric and generic systems. We will denote n_m^i associated with symmetric systems as n_s, and n_m^i associated with generic systems as n_g.

Strips [Fig. 3.3(a)]. — From Table 3.1 we infer that $1\times N_x$ and $2\times N_x$ strips are always floppy, as the balance $n_m^i - n_{ss}$ is positive. Moreover, since these strips have no states of self-stress, the number of zero modes for generic and symmetric strips are equal. For $N_y = 1$, the number of zero modes increases with N_x as $n_s = n_g = N_x - 1$. Interestingly, for $N_y = 2$, strips exhibit a single zero mode ($n_s = n_g = 1$), independently of N_x. This internal zero mode is characterized by the hinging motion of quads, as depicted by the coloured arrows in Fig. 3.3(a). This hinging mode will be described in more detail in section 3.2.2.

Clusters of size 3×3 or larger [Fig. 3.3(b)]. — For $N_y = 3$ and $N_x \geq 3$, the balance $n_m^i - n_{ss}$ becomes less than or equal to 0. The system then

only can attain zero modes if a sufficient number of states of self-stress are present. Let us first inspect $N_x = 3$. Here, $n_m^i - n_{ss} = 0$, and for generic clusters both n_g and n_{ss} are zero — the system is isostatic. In contrast, for symmetric clusters, there is always one hinging mode, and n_s equals one, implying that the system also has a state of self-stress. For generic clusters, with $N_x > 3$ and $N_y = 3$, we have $n_g = 0$, $n_{ss} = N_x - 3$; for symmetric clusters of the same size, $n_s = 1$, $n_{ss} = N_x - 2$. More generally, the outcome $n_s = 1$ and $n_g = 0$ persists irrespective of the cluster size, provided $N_x, N_y \geq 3$. This suggests that symmetric clusters attain extra states of self-stress in comparison to generic clusters in order to maintain the balance $n_m^i - n_{ss}$ for a given system.

Looped strips [Fig. 3.3(c)]. — As a third geometry, we consider looped-strips. Their rigidity is most easily understood by regarding it as a strip whose head and tail are connected by two extra bonds. Let us first consider the case before quadrilaterals *i* and *ii* are present; then, $n_s = n_g = 1$ and $n_{ss} = 0$.

When we add quad *i* in the symmetric case, we add 3 degrees of freedom, as well as 4 constraints; since n_s remains 1, this implies we create one state of self-stress. Adding quad *ii* then adds 3 degrees of freedom and 6 constraints; n_s remains one, and n_{ss} becomes 4. In the generic case, the solution is different. Consider the two corners of the quads that would connect to quad *i*. In the generic case, their motions are not correlated, and their distance will be variable. Hence, connecting these corners with quad *i*, the system becomes rigid — $n_g = 0$ and the counting then specifies that $n_{ss} = 0$ as well. Adding quad *ii* then yields $n_g = 0$ and $n_{ss} = 3$.

The 3×3 (or larger) clusters and the looped-strips discussed above illustrate a general observation. For the generic case, strip-like configurations have $n_g = 1$ and $n_{ss} = 0$; think of the looped-strip without quads *i* and *ii*, but also of a 3×3 cluster with one corner removed. Once there is a loop, generic systems become rigid $(n_g = 0)$, but symmetric systems maintain their hinging mode $(n_s = 1)$, implying that these always feature additional states of self-stress. Moreover, loops and sufficiently large clusters thus induce differences between n_s of symmetric systems and n_g of generic systems.

3.2 System and methods

In this section we set up the mathematical description for (diluted) collections of rigid quads that are connected by flexible hinges, and review the basic ingredients of zero mode counting. In section 3.2.1 we present the mathematical framework which covers both symmetric systems featuring regular, identical squares, and generic systems featuring irregular quads. Furthermore, we discuss the procedure to construct stress-free generic systems by the application of small geometric perturbations to symmetric systems. In section 3.2.2 we distinguish two types of zero modes; mechanisms and quartic modes. Section 3.2.3 briefly reviews the standard technique used to count the number of zero modes of symmetric and generic systems. Finally, section 3.2.4 discusses how we choose the magnitude of the perturbations to properly count excess zero modes from numerical simulations.

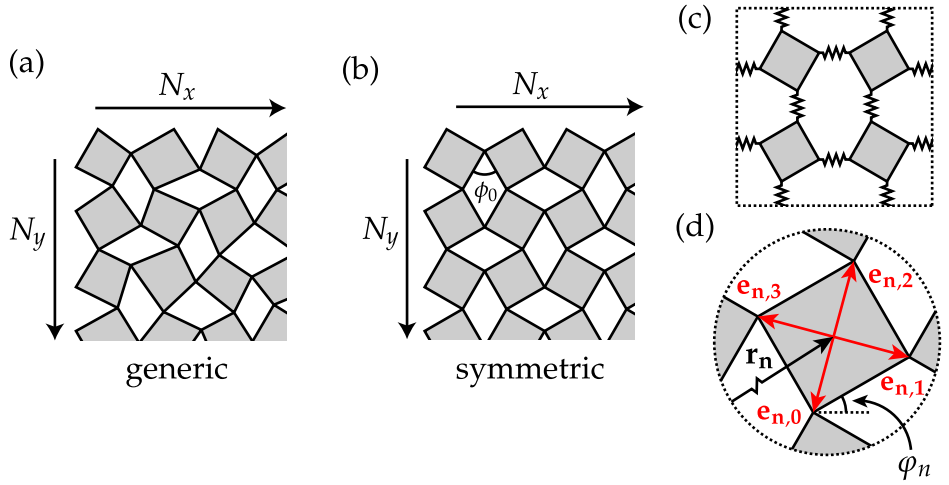

Figure 3.4: System definitions. (a) Generic and (b) symmetric systems of size $N_x \times N_y$. The opening angle between adjacent squares in symmetric systems is denoted ϕ_0. (c-d) Connectivity and quad description; these are shown for a symmetric system, but equally apply to generic systems. (c) Hinges are modelled by linear springs of zero rest length which connect the corners of adjacent quads. Upon relaxation of the springs, the quads' corners coincide. (d) The coordinate system used to describe the shape, position and orientation of individual quads (see main text).

3.2.1 Mathematical description

To study collections of rigid quads connected by flexible hinges, we model these systems as $N_x \times N_y$ lattices of rigid quads connected by springs of unit stiffness and zero rest length [Fig. 3.4]. Unless noted otherwise, we use open boundary conditions, motivated by the goal to obtain designs for finite-sized metamaterials. For full filling, our systems contain a total of $N_t = N_x N_y$ quads and $N_b = 2N_x N_y - (N_x + N_y)$ springs (bonds), where the non-extensive correction term $N_x + N_y$ stems from the missing bonds of the quads located at the boundaries. For very large systems, the number of bonds approaches $2N_x N_y \left[1 - (N_x + N_y)/(2N_x N_y)\right] \approx 2N_x N_y$, indicating that each quad is connected to 4 neighbouring quads. Note that the terms hinges, springs and bonds are used synonymously in this thesis — these terms should all be interpreted similarly.

Quad description and state vector. — To mathematically describe our systems, we assign each of the $N_x N_y$ quads a label, n, along with a centre location $\mathbf{r_n} = (x_n, y_n)$, a rotation angle φ_n, and the centre-to-corner vectors $\mathbf{e_{n,i}}$ $(i = 0,1,2,3,4)$ [see Fig. 3.4(d)]. Note that $\mathbf{e_{n,i}}$ therefore specifies the shape of each quad.

Quads are modelled as rigid objects, implying that their shape remains fixed when the system is deformed. In contrast, $\mathbf{r_n}$ and ϕ_n might change for a given deformation. Having prescribed the shape of the quads, we can therefore fully characterize our systems by the state vector

$$\mathbf{X} = (x_1, y_1, \varphi_1, x_2, y_2, \varphi_2, ...x_N, y_N, \varphi_N)^T, \tag{3.5}$$

which is a $3N \times 1$ vector providing the centre location and rotation angle of each quad.

To build symmetric systems, we use squares of side length 1, which are described by perpendicular centre-to-corner vectors $(\mathbf{e_{n,i}} \perp \mathbf{e_{n,i+1}})$ of magnitude $\sqrt{2}/2$. The centres of the squares are then stacked on a square-like, two-dimensional grid, such that the corners of adjacent squares coincide, as in Fig. 3.4(b). Note that the grid spacing controls the opening angle ϕ_0 between adjacent squares, which is related to the rotation angle of a single square as $\varphi_n = \pm\phi_0/2$. Here, the sign of φ_n depends on the alternating counter or clockwise rotation of quad n. The procedure to build generic systems is different. In these disordered systems, the shape and

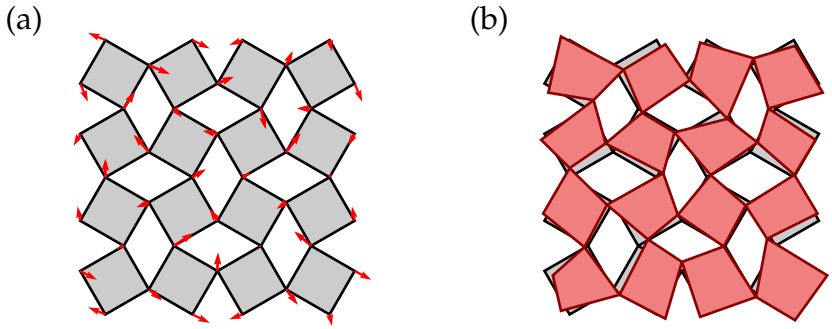

Figure 3.5: Procedure to construct stress-free, generic systems. (a) Starting from a symmetric system, we randomly displace connected corners by a random vector $\mathbf{\Delta e_{n,i}}$, as visualized by the red arrows. Here we have used $\epsilon = 0.3$ and to enhance visualization the magnitude of the resulting vectors is shown at 200%. (b) The resulting generic system (red), superimposed on the symmetric system.

orientation of quads is arbitrary and the corners of adjacent quads generally do not coincide. In the paragraph hereafter we will motivate and discuss the procedure to construct arbitrary generic systems for which the corners of adjacent quads exactly coincide [e.g. as in Fig. 3.4(d)].

Generic, stress-free systems. — We now discuss the procedure to construct stress-free generic systems. In such systems, the corners of adjacent quads coincide and the springs are not pre-stressed. The design of such systems is motivated by the significant simplification of the mode counting analysis described in section 3.2.3. Stress-free systems allow for the random removal of quads while retaining equilibrium, but if pre-stresses would be present, quad removal could initiate the relaxation to a lower energy state. This would require the calculation of intermediate equilibrium configurations with the aid of computationally time-consuming conjugate gradient techniques — stress-free systems circumvent the need for such techniques. Note that, as mentioned already, symmetric systems are automatically stress-free due to the non-generic nature of the squares.

To construct the stress-free, generic systems we systematically perturb symmetric systems by randomly displacing connected corners, as is illustrated in Fig. 3.5. This procedure stretches no springs and thus ensures no pre-stresses develop when changing the squares to irregular quads.

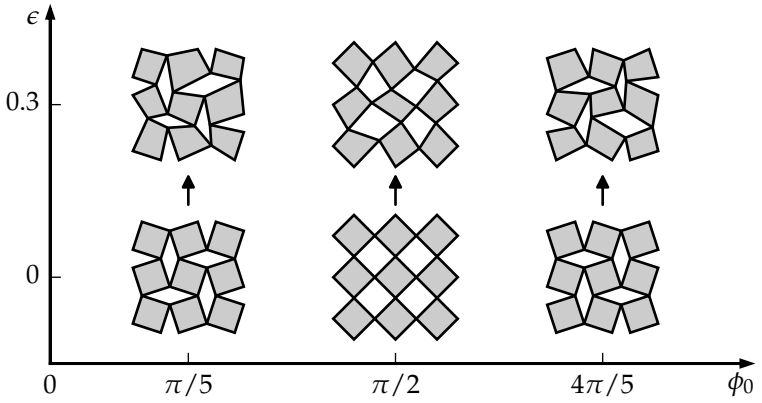

Figure 3.6: Stress-free, generic systems obtained by perturbing symmetric systems with magnitude ϵ, for a range of symmetric opening angles. Note that the top systems do not feature zero modes.

To quantify the magnitude and direction of the random displacements, we use the random vectors $\mathbf{\Delta e_{n,i}} = \left(\epsilon_x, \epsilon_y\right)^T \|\mathbf{e_{n,i}}\|$ (red arrows in Fig. 3.5). The centre-to-corner vectors of the perturbed generic quads then readily follow from the vectorial sum $\mathbf{e'_{n,i}} = \mathbf{e_{n,i}} + \mathbf{\Delta e_{n,i}}$, where we note that $\mathbf{e_{n,i}}$ is associated with the initial symmetric system. Furthermore, ϵ_x and ϵ_y represent random numbers sampled from a uniform probability distribution that lie within the interval $[-\epsilon, \epsilon]$. In the following section we will demonstrate that $\epsilon = 0.1$ is a suitable choice to detect excess zero modes (the modes that only occur in symmetric systems). Finally, Fig. 3.6 shows some more examples of generic systems, obtained by perturbing symmetric systems of different opening angles. In the remainder of this work we utilize the technique as described here to construct stress-free, generic systems.

The energy of the system, E. — The systems introduced in Fig. 3.4 contain N_b springs of unit stiffness and rest length zero. This yields the following expression for the total energy of a system

$$E\left(\mathbf{X}\right) = \frac{1}{2} \sum_{s=1}^{N_b} \ell_s \left(\mathbf{X}\right)^2, \tag{3.6}$$

with ℓ_s the length of spring s. As mentioned before, for fully filled systems (no quads removed), $N_b = 2N_xN_y - (N_x + N_y)$, but this number will be lower in diluted systems. More importantly, it should be noted that the springs lengths are a function of the state vector $\mathbf{X}$; for the undeformed symmetric and (stress-free) generic systems no springs are stretched, hence $E(\mathbf{X}) = 0$. When applying a deformation $\mathbf{X}$ changes and E might change as well. For deformations associated with a zero mode, $E(\mathbf{X})$ remains unchanged up to quadratic order. In contrast, applying deformations that are not associated with zero modes lead to a quadratic increase of $E(\mathbf{X})$. The actual ℓ_s that correspond to a given $\mathbf{X}$ are calculated numerically by subtracting the corner positions of adjacent quads, which are easily calculated by combining $\mathbf{e_{n,i}}$ with $\mathbf{X}$. In section 3.2.3 we will use $E(\mathbf{X})$ to construct the Hessian matrix, which forms the basis of counting zero modes.

3.2.2 Finite amplitude and quartic modes

The zero modes we encounter in this work can be subdivided in two types of zero modes: Finite amplitude mechanisms and quartic modes. A mechanism is a 'finite' zero mode in which finite-amplitude displacements of quadrilaterals stretch no springs. A quartic mode is an infinitesimal zero mode in which spring lengths do not change to first order in the magnitude of quadrilateral displacements, $\mathbf{\Delta X}$, but do so to second order. In the latter case, the energy changes with the quadrilateral displacements as $\mathbf{\Delta X}^4$, hence the name quartic mode. Below we provide examples of a mechanism and quartic mode.

Global hinging. — The mechanism we focus on in this paragraph – global hinging– occurs for arbitrary large symmetric systems with open boundary conditions. For symmetric systems, the centre coordinates of the squares compose a square lattice, thereby allowing for a collective counter rotating motion of the squares without stretching bonds. This collective motion is illustrated in Fig. 3.7(a), using $\phi_0 \in [0, \pi]$ as the control parameter. From these snapshots we observe a non-monotonic unfolding of the tiling for increasing ϕ_0: Starting from a nearly closed system ($\phi_0 = \pi/20$), the system unfolds to maximum opening ($\phi_0 = \pi/2$), and then shrinks again towards the nearly closed system ($\phi_0 = 19\pi/20$). Since this

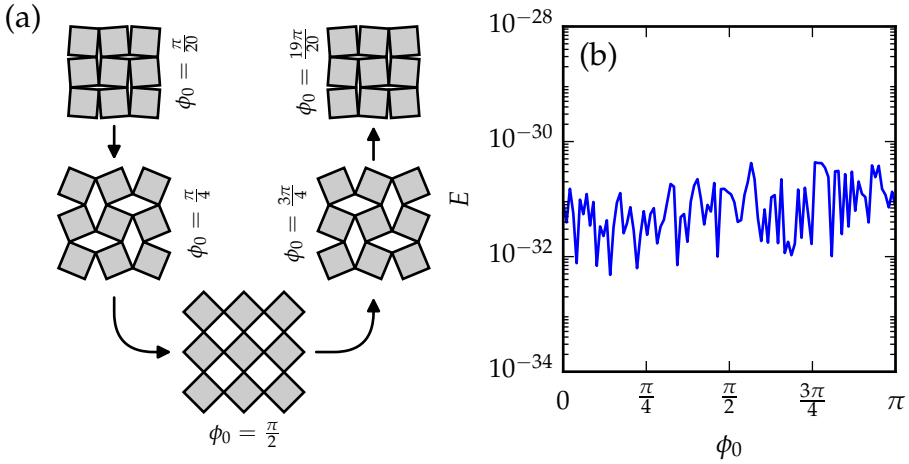

Figure 3.7: Global hinging mode in a symmetric 3×3 system. In this mode the opening angle ϕ_0 can be varied over a finite amplitude without stretching the bonds. (a) Subsequent snapshots of the tiling when varying ϕ_0 from $\pi/20$ to $19\pi/20$. Note that the hinging behaviour for $\phi_0 < \pi/2$ and $\phi_0 > \pi/2$ is related by symmetry. (b) The numerically obtained energy as function of the opening angle ϕ_0.

collective motion of squares relies on hinging and involves a global shape change, we refer to this mode as *global hinging*.

To confirm that no springs are stretched during the global hinging, we have plotted the energy as function of ϕ_0 in Fig. 3.7(b). The energy remains zero (within numerical precision) over the complete range of ϕ_0, and thus reflects that global hinging of symmetric systems is a mechanism.

Finally, we anticipate that the global hinging mode ceases to exist for generic systems, as the underlying square lattice becomes distorted for finite ϵ. This will be confirmed in section 3.2.4, in which we reveal the energy increase of the global hinging mode with ϵ.

Quartic and finite energy modes. — In Fig. 3.8(a) we display an example of spurious quartic modes that occur in symmetric systems with opening angle $\phi_0 = \pi/2$. Due to the symmetry that arises at this opening angle, the two centre squares can undergo a counter rotating motion while the vertical distance y_q is preserved to leading order in the side-

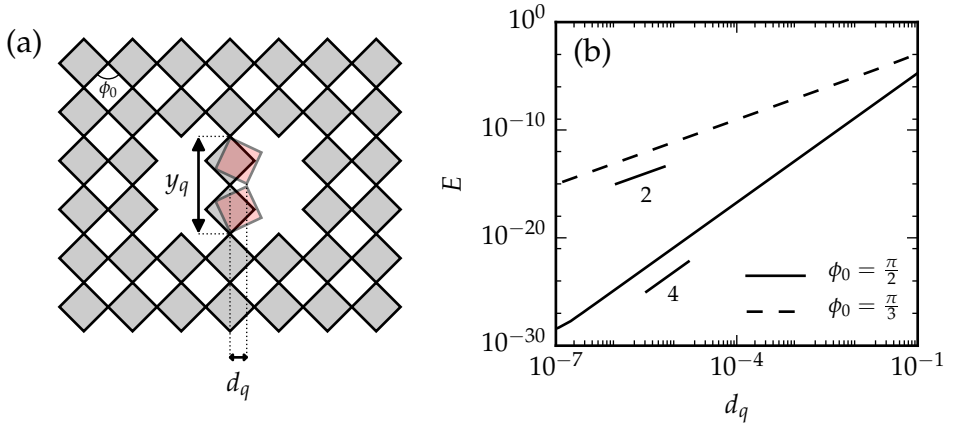

Figure 3.8: Quartic modes in symmetric systems. (a) For $\phi_0 = \pi/2$ the two centre squares can deflect to the right (coloured red), or equally to the left (not shown), while y_q is preserved to leading order in the sidewards deflection d_q. (b) The energy change of this mode as function d_q shows clear powerlaw behaviour with exponent 4 for $\phi_0 = \pi/2$ (solid line), and exponent 2 for $\phi_0 = \pi/3$ (dashed line).

wards deflection d_q. The energy change associated with d_q is plotted in Fig. 3.8(b) (solid line) and shows clear powerlaw behaviour with exponent 4, confirming the zero mode is quartic in nature.

To suppress the spurious quartic modes, we set $\phi_0 = \pi/3$ in the remainder of this work. This (arbitrary) choice destroys the symmetry that arises in symmetric systems for $\phi_0 = \pi/2$ and kills the quartic modes related to this symmetry. This is verified by plotting the energy change associated with d_q for $\phi_0 = \pi/3$ in Fig. 3.8(b) (dashed line), which now shows powerlaw behaviour with exponent 2 rather than exponent 4. The exponent 2 demonstrates that the springs lengths are changing to first order in the magnitude of the quadrilateral displacements (here expressed as d_q) and this exponent is common for finite energy modes. Even though we kill quartic modes related to the opening angle ϕ_0 by setting $\phi_0 = \pi/3$, quartic modes originating from more complex symmetries, although rare, can still appear in diluted symmetric systems (see chapter 4 for examples). The appearance of these quartic modes is inevitable and in the remainder of this thesis we do not distinguish between mechanisms and quartic modes, unless explicitly noted otherwise.

3.2.3 Mode counting

We now discuss the technique to detect the number of zero modes and their spatial structure. For a given tiling in some reference state $\mathbf{X}$ [Eq. (3.5)], deformations associated with zero modes, $\Delta\mathbf{X}$, leave the energy E unchanged up to quadratic order in $\Delta\mathbf{X}$. To find all $\Delta\mathbf{X}$ that satisfy this criterium, the approach is to analytically expand the energy around state $\mathbf{X}$, which yields a matrix equation that can be numerically diagonalized.

Starting with the expansion of the energy in Eq. (3.6) about $\mathbf{X}$ up to quadratic order, we obtain

$$E(\mathbf{X}+\boldsymbol{\Delta}\mathbf{X}) = E(\mathbf{X}) + \boldsymbol{\Delta}\mathbf{X}^T \nabla E(\mathbf{X}) + \frac{1}{2}\boldsymbol{\Delta}\mathbf{X}^T \mathbf{H}(\mathbf{X})\,\boldsymbol{\Delta}\mathbf{X}, \tag{3.7}$$

with $\nabla E(\mathbf{X})$ the gradient and $\mathbf{H}(\mathbf{X})$ the Hessian matrix of the energy evaluated at $\mathbf{X}$. The gradient $\nabla E = \partial E/\partial \mathbf{X}$ is a $3N_xN_y \times 1$ vector that contains all first derivatives of the energy with respect to the quadrilateral positions and orientations,

$$\nabla E = \left[\frac{\partial E}{\partial x_1}, \quad \frac{\partial E}{\partial y_1}, \quad \frac{\partial E}{\partial \varphi_1}, \quad \ldots, \quad \frac{\partial E}{\partial \varphi_{N_t}}\right]^T. \tag{3.8}$$

The Hessian is a $3N_xN_y \times 3N_xN_y$ matrix that contains the second derivatives of the energy with respect to the entries of $\mathbf{X}$, which yields

$$\mathbf{H} = \begin{bmatrix} \frac{\partial^2 E}{\partial x_1^2} & \frac{\partial^2 E}{\partial x_1 \partial y_1} & \frac{\partial^2 E}{\partial x_1 \partial \varphi_1} & \cdots & \frac{\partial^2 E}{\partial x_1 \partial \varphi_{N_t}} \\ \frac{\partial^2 E}{\partial y_1 x_1} & \frac{\partial^2 E}{\partial^2 y_1} & \frac{\partial^2 E}{\partial y_1 \partial \varphi_1} & \cdots & \frac{\partial^2 E}{\partial y_1 \partial \varphi_{N_t}} \\ \frac{\partial^2 E}{\partial \varphi_1 \partial x_1} & \frac{\partial^2 E}{\partial \varphi_1 \partial y_1} & \frac{\partial^2 E}{\partial^2 \varphi_1} & \cdots & \frac{\partial^2 E}{\partial \varphi_1 \partial \varphi_{N_t}} \\ \vdots & \vdots & \vdots & \ddots & \vdots \\ \frac{\partial^2 E}{\partial x_{N_t} \partial x_1} & \frac{\partial^2 E}{\partial x_{N_t} \partial y_1} & \frac{\partial^2 E}{\partial x_{N_t} \partial \varphi_1} & \cdots & \frac{\partial^2 E}{\partial x_{N_t} \partial \varphi_{N_t}} \end{bmatrix}. \tag{3.9}$$

The entries of the gradient and Hessian matrix are complicated functions of the quadrilateral corner coordinates $(x_{n,i}, y_{n,i})$ and the rotation angle φ_n, but can be fully determined analytically. For a detailed analytical derivation of the gradient and Hessian matrix for the systems considered in this work, we refer to appendices 3.A and 3.B.

The expansion of the energy in Eq. (3.7) can be simplified as follows. First, we focus on systems in the absence of external forces for which $\mathbf{X}$ is an equilibrium configuration satisfying $\nabla E(\mathbf{X}) = \mathbf{0}$. As such, the second term on the right hand side of Eq. (3.7) drops out. Second, due to the procedure described in section 3.2.1 systems are free of internal stresses, hence $E(\mathbf{X}) = 0$ and the first term on the right hand side drops out as well. Note that this stress-free condition also ensures the gradient $\nabla E(\mathbf{X})$ remains zero when quadrilaterals are removed. Taking both simplifications into account, the expansion [Eq. (3.7)] turns into

$$E(\mathbf{X} + \Delta\mathbf{X}) = \frac{1}{2}\Delta\mathbf{X}^T\mathbf{H}(\mathbf{X})\Delta\mathbf{X}. \tag{3.10}$$

Then, to find all non-trivial $\Delta\mathbf{X}$ for which the right hand side of Eq. (3.10) is zero, we consider the eigenvectors and associated eigenvalues of the matrix $\mathbf{H}$. Any of such eigenvectors $\Delta\mathbf{X}_{\boldsymbol{\lambda}}$ has the special property to preserve direction when multiplied by $\mathbf{H}$, but to be multiplied by a scalar λ, the associated eigenvalue [123]. More formally, $\mathbf{H}(\mathbf{X})\Delta\mathbf{X}_{\boldsymbol{\lambda}} = \lambda\Delta\mathbf{X}_{\boldsymbol{\lambda}}$, and substitution in Eq. (3.10) yields

$$E(\mathbf{X} + \Delta\mathbf{X}_{\boldsymbol{\lambda}}) = \frac{1}{2}\lambda\|\Delta\mathbf{X}_{\boldsymbol{\lambda}}\|^2, \tag{3.11}$$

which demonstrates that for $\lambda = 0$ the energy is unaltered under a deformation $\Delta\mathbf{X}_{\boldsymbol{\lambda}}$. Hence, eigenvectors with associated eigenvalue $\lambda = 0$ are zero modes. While the Hessian can be determined analytically, the $3N_xN_y$ eigenvalues and eigenvectors need to be determined numerically. In our numerics (double precision) a zero mode typically has $\lambda = \mathcal{O}(10^{-16})$, which is sufficient to distinguish zero modes from finite-energy modes. We will elaborate in more detail on this aspect in the following section.

3.2.4 Magnitude of ϵ and numerical zero modes

For systems consisting of perfect squares, there is a global hinging zero mode (section 3.2.2) — in generic systems consisting of perturbed quadrilaterals, this mode attains a finite energy, and should not be counted as

a zero mode. Once we dilute these systems, new zero modes can arise. In this section we describe how we numerically distinguish zero modes from finite energy modes. In particular we motivate our choice for the magnitude of the perturbations in generic systems and the criterium we use to distinguish zero from non-zero eigenvalues. We show that perturbations with magnitude $\epsilon = 0.1$ and a cut-off criterium for the eigenvalues $\lambda_c = 10^{-10}$ suffice to unambiguously detect the zero modes of both generic and symmetric systems. In the remainder of this section we use $N_x = N_y = 10$ to exemplify our choices.

We now first elaborate on our choice for the magnitude of ϵ. To this end, we determine the eigenvalues of fully-filled, generic systems when varying ϵ over 8 orders of magnitude. We present results using a single simulation per value of ϵ, because we found (from comparison of multiple simulations per ϵ) that their outcome exhibits only very minor scatter (not shown here). Using single simulations for each ϵ, we have visualized the eigenvalues as function of ϵ in Fig. 3.9(a). From this plot we observe that for each value of ϵ, there exists a cluster of eigenvalues with λ of order 1, there are 3 eigenvalues of order 10^{-15}, and in between there is a single eigenvalue, λ_h, whose value exhibits power law behaviour: $\lambda_\mathrm{h} \sim \epsilon^2$. The scaling exponent 2 is very robust and does not depend on the particular value $\phi_0 = \pi/3$ chosen here, but holds for any opening angle within the accessible range.

In terms of eigenmodes, the clusters of eigenvalues at the top are associated with finite energy eigenmodes, while the eigenvalues at the bottom are associated with the three trivial, global eigenmodes of the systems: x-translation, y-translation and rotation. The eigenvalue λ_h arises from the global hinging mode and becomes increasingly smaller as the perturbations decrease. Note that this is what one would expect, since the centre locations of the quadrilaterals converge towards a perfect square lattice for decreasing ϵ. Therefore, the global hinging motion becomes increasingly 'softer' and eventually λ_h becomes of the same order as the eigenvalues associated with the three trivial eigenmodes. Furthermore, the scaling between λ_h and ϵ with exponent 2 can quantitatively be understood by noticing that quadrilateral rotations in generic systems, that arise due to global hinging, involve changes in spring length of order ϵ. Hence, the corresponding change in energy scales as ϵ^2, implying that $\lambda_h \sim \epsilon^2$ by Eq. (3.11).

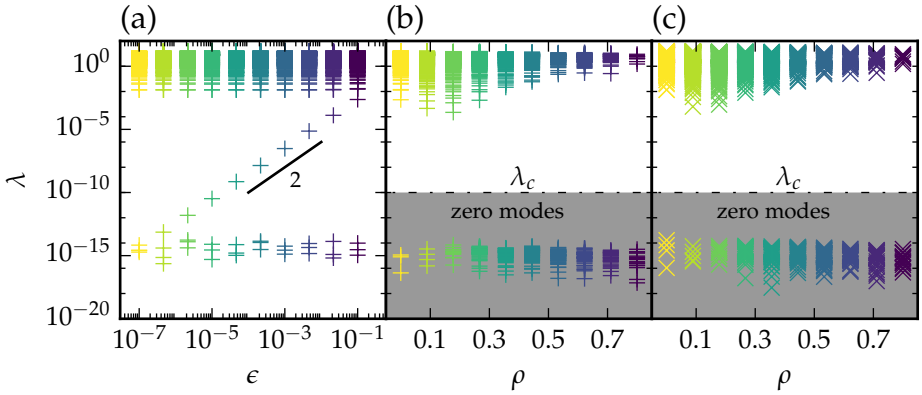

Figure 3.9: Eigenvalues of the Hessian for $N_x = N_y = 10$ and $\phi_0 = \pi/3$. (a) For a fully-filled, generic system, we plot the eigenvalues for varying ϵ. Each color shows the distribution of the $3N_xN_y$ eigenvalues that belong to a given ϵ. (b-c) Eigenvalues for diluted systems as function of the cutting fraction ρ. Here, each colour is associated with the eigenvalues that belong to a given ρ. We consider eigenvalues smaller than $\lambda_c < 10^{-10}$ as zero modes, indicated by the shaded regions. In (b) we show results for generic systems ($\epsilon = 0.1$) and in (c) for symmetric systems ($\epsilon = 0$).

The trivial eigenmodes —global translations or rotation— involve no energy penalty, allowing us to infer from Fig. 3.9(a) that our numerical precision for a zero mode is of order 10^{-15}. Hence, to ensure that the hinging mode attains a finite energy in generic systems, and is not counted as a zero mode, we pick ϵ such that λ_h in generic systems remains orders of magnitude separated from the order 10^{-15}. Therefore, we set $\epsilon = 0.1$ in the remainder of this work. The resulting clear separation in eigenvalues of zero modes versus finite-energy modes occurring for $\epsilon = 0.1$ allows us to define a critical eigenvalue λ_c in order to count the number of zero modes. Using λ_c as a cut-off criterium, we count eigenvalues below λ_c as zero modes, but eigenvalues above λ_c as finite energy modes. Fig. 3.9(a) illustrates that $\lambda_c = 10^{-10}$ is suitable for systems of full filling.

We conclude this section by showing that this cut-off approach remains valid for diluted systems. To study the distribution of eigenvalues in diluted systems, we randomly remove $N_r = \rho N$ quadrilaterals and determine the eigenvalues of the remaining system. We use a single simulation per value of ρ, because we found that, similar to the eigenvalue

study for varying ϵ, eigenvalues exhibit only minor scatter for random dilution (not shown here). In Fig. 3.9(b-c) we have plotted the eigenvalues as function of the cutting fraction ρ using a single simulation per value of ρ, both for generic (panel b) and non-generic systems (panel c). This demonstrates that for increasing ρ new zero modes start to appear, and more importantly, that the clear separation in eigenvalues of zero and finite-energy modes persists over the range of ρ. Hence, $\lambda_c = 10^{-10}$ is also a valid cut-off criterium for diluted systems. In summary, we have motivated the choices $\epsilon = 0.1$ and $\lambda_c = 10^{-10}$ to distinguish true zero modes from finite energy modes, and in the remainder of this work we will use these values.

3.3 Random quad removal

In this section we determine the number of zero modes in generic (n_g) and symmetric (n_s) systems for random quad removal. In section 3.3.1 we present the phenomenology of random quad removal, demonstrate that n_s can exceed n_g, and present the spatial structure of such excess zero modes. In section 3.3.2 we fully characterize the number of excess zero modes as function of system size and the fraction of removed quads, and show that the mean number of excess zero modes exhibits finite size scaling with mean field exponents.

In what follows we consider systems of square periphery and initial full-filling, that is $N_x = N_y = N$ with a total number of N^2 quads. Furthermore, we use the parameter values $\phi_0 = \pi/3$, $\epsilon = 0.1$ and $\lambda_c = 10^{-10}$, as motivated in section 3.2.

3.3.1 Phenomenology

This section presents the phenomenology of random quad removal. To dilute symmetric and generic systems, we randomly remove $N_r = \rho N^2$ quads, where ρ denotes the fraction of removed quads.

Starting with fully filled systems of size $N = 10$, we track the number of zero modes in generic (n_g) and symmetric (n_s) systems for the subsequent removal of quads, when using the same ensemble of dilution patterns for both. In Fig. 3.10(a-b) we show the outcome of n_s and n_g, and their ensembles averages $\langle n_s \rangle$ and $\langle n_g \rangle$, as function of the cutting fraction

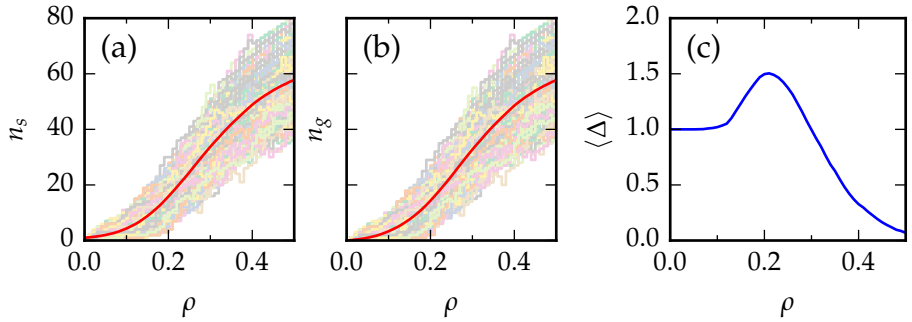

Figure 3.10: Random quad removal in 10×10 systems. (a-b) The number of zero modes in symmetric (n_s) and generic (n_g) systems as function of the cutting fraction ρ. Each panel displays the outcome of 10^3 independent cutting sequences (curves of low brightness) along with the ensemble averages $\langle n_s \rangle$ and $\langle n_g \rangle$ (red curves of high brightness). (c) Subtracting $\langle n_g \rangle$ from $\langle n_s \rangle$ yields the average number of excess zero modes, $\langle \Delta \rangle$.

ρ, for 10^3 independent cutting sequences. As can be observed, n_s and n_g generally increase with ρ, but might incidentally decrease [see lower curves in Fig. 3.10(a-b)] when a quad associated with a given zero mode is removed — a simple example being a quad that is only connected at one corner. The growth of the ensemble averages $\langle n_s \rangle$ and $\langle n_g \rangle$ [solid red curves in Fig. 3.10(a-b)] appear nearly identical, and to reveal differences between symmetric and generic systems we introduce

$$\langle \Delta \rangle = \langle n_s - n_g \rangle. \tag{3.12}$$

This quantity corresponds to the number of extra zero modes that exist in symmetric, but not in generic systems, due to the non-generic nature of the squares. Therefore, we refer to Δ as the number of *excess zero modes*. Interestingly, $\langle \Delta \rangle (\rho)$ [Fig. 3.10(c)], reveals subtle but important differences between symmetric and generic systems. Whereas $\langle \Delta \rangle = 1$ for nearly fully filled systems ($\rho \approx 0$), due to the global hinging mode that is present in symmetric but absent in generic systems, $\langle \Delta \rangle = 0$ for strongly diluted systems ($\rho \to 1$). The latter limit will be clarified in chapter 4, where we show this to be due to an absence of sufficiently large clusters of connected quads. Surprisingly, for intermediate cutting fractions, $\langle \Delta \rangle$ exhibits a peak and exceeds 1, showing that there exist dilution patterns for which $n_s - n_g \geq 2$.

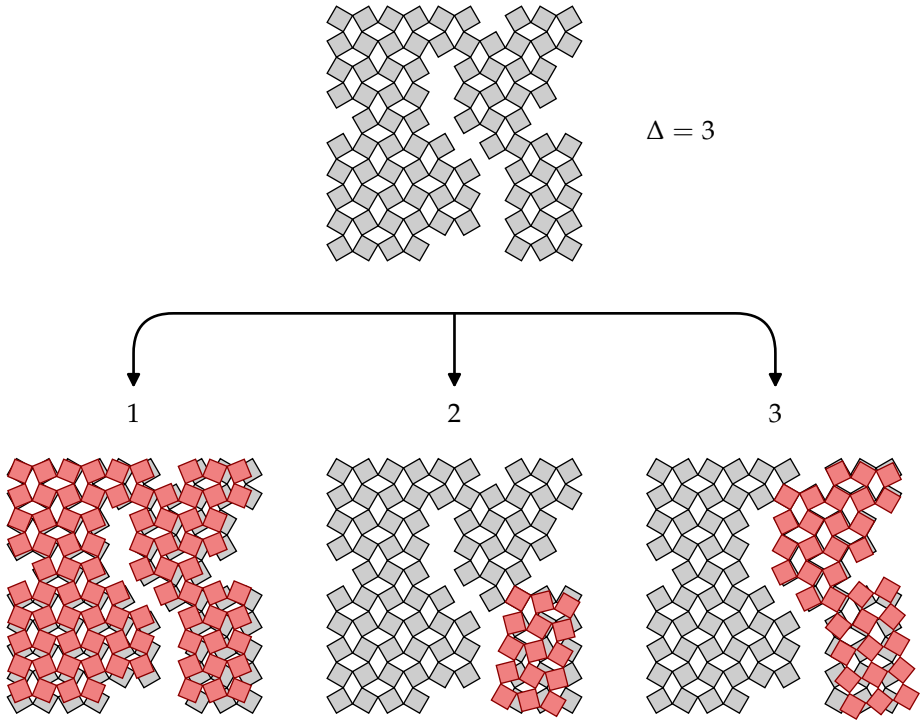

Figure 3.11: Spatial structure of excess zero modes. The randomly diluted 10×10 system ($\rho = 0.16$) shown at the top row has $n_s = 3$ and $n_g = 0$. The bottom row visualizes the spatial motions of the excess zero modes by superimposing the deformed geometry in red. To exclude additional displacements from global translations and/or rotations to these excess modes, the (x,y) position of the upper left square and the y position of the square directly next to it are held fixed (as might be noticed from mode 1).

We now illustrate the spatial structure of some excess zero modes. The particular cutting pattern shown in Fig. 3.11 features three excess zero modes, each of which has been visualized by extracting the associated displacement vector $(\Delta \mathbf{X})$ from the eigenmode analysis. Mode (1) can be recognized as the global hinging mode, whereas (2) and (3) are more complex and rely on the (oblique) sub-hinging of the individual clusters coloured in red. The observed sub-hinging of clusters plays, as we will show, a central role for excess zero modes.

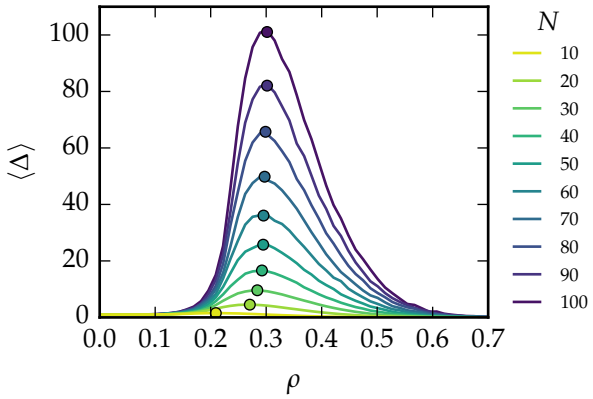

Figure 3.12: Statistics of the excess zero modes. For increasing system size N we have determined the multitude of excess zero modes as function of the cutting fraction. The maximum of each curve is marked by a filled circle.

3.3.2 The multitude of excess zero modes

We now reveal the multitude of excess zero modes $\langle\Delta\rangle$ as function of system size and cutting fraction. In Fig. 3.12 we show $\langle\Delta(\rho,N)\rangle$ for system sizes $N = 10,20,30,\ldots,90,100$, where we indicate the maximum of each curve by a filled circle. The number of runs needed to obtain reasonably well statistically converged curves decreases with N. To quantify the statistical convergence, we use the relative variance of Δ at the maximum as a criterium and demand $\sigma < 0.01\%$. The number of runs that follows from this criterium is subsequently also used for other values of ρ (at fixed N). In particular, using $\sigma^2 < 0.01\%$, we have found that an ensemble of typically 1100 simulations is required for $N = 20$, while an ensemble of only 100 simulations is sufficient for $N = 100$. The lower number of runs required for larger system sizes presumably is a result of spatial self-averaging, in which large systems can be regarded as a collection of smaller subsystems that are sufficiently uncorrelated.

Upon close inspection of the maxima in Fig. 3.12, we can make two observations. First, the location of the maximum, $\rho^{\max}$, increases with the system size and eventually converges to $\rho \approx 0.3$. Second, the value of the maximum, $\langle\Delta\rangle^{\max}$, grows with the system size, and becomes as large as $\langle\Delta\rangle^{\max} \approx 100$ for the largest system size considered. To characterize the

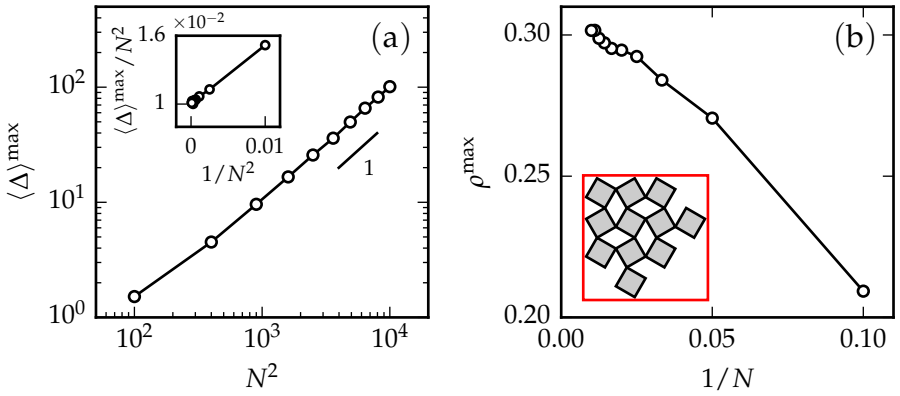

Figure 3.13: Peak behaviour of $\langle\Delta\rangle(\rho)$. For the data shown in Fig. 3.12, we have determined the value and location of the peak with system size. (a) The value of peak grows linearly with N^2 for large N (log scale, slope 1), implying that $\langle\Delta\rangle^{\max} \sim N^2$. Inset (linear scale): For small N, the scaling $\langle\Delta\rangle^{\max} \sim N^2$ exhibits finite size corrections proportional to $1/N^2$. (b) The peak location tends to a constant as $1/N$. Inset: Unit cell to understand the value of ρ_∞ (see main text).

behaviour of the maximum in detail, we measured $\rho^{\max}$ and $\langle\Delta\rangle^{\max}$ for each system size, where we refined our $\langle\Delta\rangle(\rho)$ data by a quadratic fit in the vicinity of the maximum. In Fig. 3.13 we show the obtained results for the value and position of the peak, from which we infer that

$$\langle\Delta\rangle^{\max} \approx \langle\Delta\rangle^{\star} := \beta\left(1 + \alpha/N^2\right)N^2, \tag{3.13a}$$

and

$$\rho^{\max} \approx \rho^{\star} := \rho_\infty - \gamma/N, \tag{3.13b}$$

where $\alpha \approx 51$, $\beta \approx 0.01$ and $\gamma \approx 0.99$ denote proportionality constants, and $\rho_\infty \approx 0.31 \pm 0.01$ the peak location in the $N \to \infty$ limit. We have determined the values of these constants by fitting Eqs. (3.13) to our data. The terms proportional to α and γ should be interpreted as finite size corrections to the large N asymptotics captured by $\langle\Delta\rangle^{\star} = \beta N^2$ and $\rho^{\star} = \rho_\infty$; the values of α and γ describe the convergence towards these large N asymptotics. Note that the asymptotic scaling $\langle\Delta\rangle^{\star} = \beta N^2$ implies that the mean number of excess zero modes in the peak regime is an intrinsic quantity, indicating roughly one extra excess zero mode for each 100

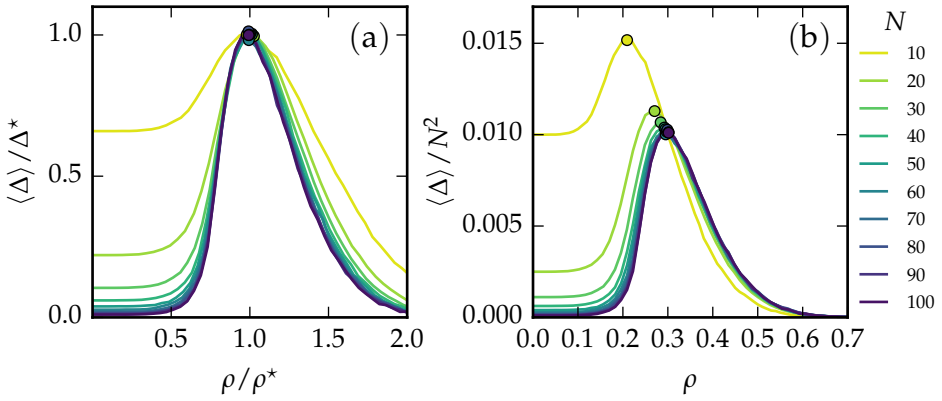

Figure 3.14: Scaling collapses for the $\langle\Delta\rangle(\rho)$ curves in Fig. 3.12. (a) Collapses obtained by rescaling the axes with $\rho^\star$ and $\Delta^\star$ (see main text), using $\alpha = 0.55$, $\beta = 0.01$, $\rho_\infty = 0.31$ and $\gamma = -0.97$. (b) The asymptotic evolution of the curves $\langle\Delta\rangle(\rho)/N^2$ for large N illustrate that, in leading order, $\langle\Delta\rangle$ scales as N^2 and ρ tends to a constant.

quads. The fact that there is a peak, its location, and the corresponding spatial structures can be understood by considering periodic samples with many small clusters. First, the smallest clusters that yield excess zero modes are of size 3×3. We now assume that the maximum number of excess zero modes is obtained by filling the system of given size N with a large number of 3×3 clusters, connected in such a way that all (symmetric) clusters retain their internal hinging mode. The simplest and most intuitive topology that satisfies these conditions consists of 3×3 clusters separated by one column and row each, with a few quads placed on the otherwise empty rows and columns to (weakly) connect adjacent clusters. To make sure the generic system remains rigid, with the symmetric system having many hinging modes, we suggest to connect each cluster pair by two quads. The resulting unit cell of this dilution geometry [see inset of Fig. 3.13(b)] has a cutting fraction $\rho = 5/16 \approx 0.31$. This value shows a surprisingly good agreement with the peak location for random dilution in the $N \to \infty$ limit.

Finally, the relations for peak value and location in Eqs. (3.13) suggest that the mean number of excess zero modes exhibits finite size scaling, as $\langle\Delta\rangle/\langle\Delta\rangle^\star = f(\rho/\rho^\star)$. To demonstrate this, we rescale our $\langle\Delta\rangle(\rho,N)$ data

according to Eqs. (3.13), and plot the result in Fig. 3.14(a). We observe that the peak positions and values collapse, as expected, but we moreover observe that the tails of $\langle\Delta\rangle/\langle\Delta\rangle^\star$ also display a scaling collapse as $N \to \infty$, demonstrating that the mean number of excess zero modes exhibits finite sizing scaling. For completeness, Fig. 3.14(b) shows the leading order scaling collapse, $\langle\Delta\rangle/N^2$, confirming that $\langle\Delta\rangle$ scales as N^2 and ρ goes to a constant for large N.

3.3.3 Distribution of excess zero modes in the peak regime

Having presented the ensemble averages $\langle\Delta\rangle(\rho, N)$, we now focus on the ensemble distribution of excess zero modes in the peak regime of $\langle\Delta\rangle(\rho, N)$. To visualize these distributions with system size, we have determined the cumulative distribution functions (CDFs) for the ensembles of cutting sequences that correspond to $\rho = \rho^\star$ (Fig. 3.15).

The CDFs in Fig. 3.15(a) display the probability P to encounter a given Δ which is less than or equal to k times the mean $\langle\Delta\rangle^\star$. This reveals that the excess modes in the peak regime are symmetrically distributed around their mean for system sizes $\sqrt{N} \gtrsim 30$. In contrast, these appear asymmetrically distributed for smaller N due to the low number of possible excess zero modes in small systems. We furthermore observe that deviations from the mean decrease with system size; the probability to randomly encounter cutting patterns that strongly deviate from the mean is much higher in small systems as compared to large systems, due to the rapid increase of the number of possible cutting patterns with N. In Fig. 3.15(b) we have re-plotted the data in panel (a) as function of $(k-1)N$ and observe a scaling collapse for large N. According to the central limit theorem [124], the collapse demonstrates that the distribution of excess zero modes in the peak regime appears Gaussian, with standard deviation $\sigma \sim 1/N$. Note that this standard deviation implies that the number of independent measures on Δ scales with N^2, confirming our earlier hypothesis that large systems are self-averaging and may be regarded as to consist of sufficiently uncorrelated subsystems.

The findings presented here naturally raise the question how to obtain extreme designs that have significantly more excess zero modes than typical, and in section 3.4 we will develop a procedure that allows us to design geometries featuring $\Delta/\langle\Delta\rangle^\star \approx 6$, even for system sizes as large as $N = 100$.

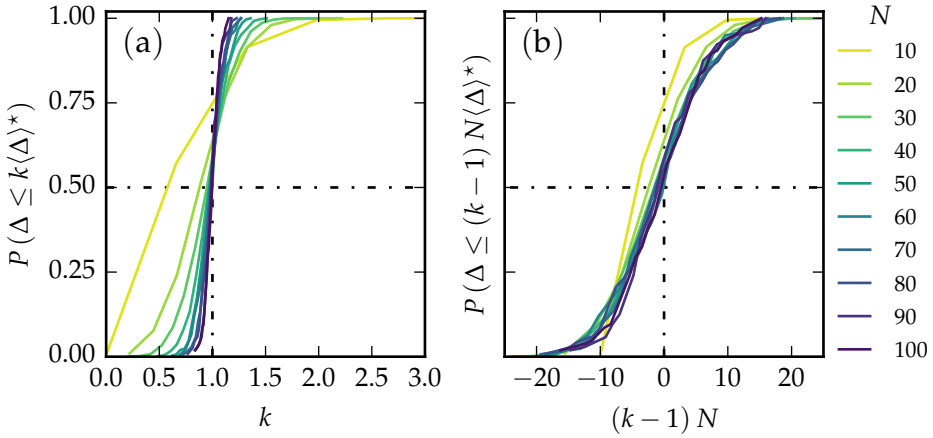

Figure 3.15: CDFs for $\Delta(\rho, N)$ in the peak regime ($\rho = \rho^{\max}$), for the data shown in Fig. 3.12. (a) The excess zero modes are symmetrically distributed around the mean $\langle\Delta\rangle^\star$ ($k = 1$) for sufficiently large system sizes. (b) Re-plotting the data shown in panel (a) as function of $(k-1)N$ results in a collapse of the curves.

3.4 Extreme systems

In this section we design systems with a large number of excess zero modes, where Δ is significantly larger than the average maximum for random cutting, $\langle\Delta\rangle^\star$. To design such systems one could follow two distinct routes. The first one consists of the brute force calculation of all possible configurations given a system size. This method is not feasible, however, as the design space is enormous: The maximum number of configurations grows exponentially with the system size and already becomes $2^{N^2} = 2^{100}$ for 10×10 systems. This number can be reduced to $\binom{100}{21} \approx 10^{21}$ by taking into account configurations at the maximum cutting fraction $\rho^\star = 0.21$ only, but the number remains enormous. Based on benchmarks of our Python based code (~ 200 iterations/s for a 10×10 system) it would take up to 10^{11} years to examine all configurations. Alternatively (the second route), one can determine the maximum Δ for a smaller, feasible system size and utilize it as an unit cell to tile the larger system — which is the approach we will use in this section.

To minimize finite size effects on the tiled system we apply periodic boundary conditions on the unit cell and consider a unit cell whose size

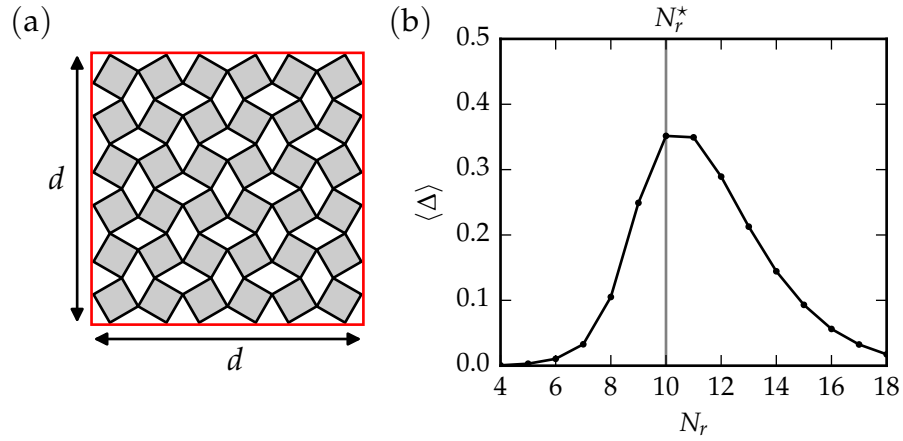

Figure 3.16: Random dilution of a 6×6 unit cell with periodic boundaries. (a) Fully filled unit cell where a fixed box size d ensures periodicity. (b) Average number of excess zero modes as function of the number of randomly removed quads for 10^6 realizations. The curve displays a maximum at $N_r = N_r^\star = 10$ as indicated by the grey line.

is as large as possible, while being computationally feasible. Based on these criteria we use a unit cell of size 6×6 $(N_u = 6)$ confined within a box of size d, as depicted in Fig. 3.16(a). Here the box size d naturally arises for periodic boundary conditions as connecting the left/right and lower/upper boundaries of the unit cell leads to a fixed opening angle ϕ_0 with corresponding box size $d = N_u\,[\cos(\phi_0) + \sin(\phi_0)]$. An important consequence of periodic boundary conditions with fixed d is that symmetric systems lose their global hinging mode, in contrast to systems with open boundaries which always have $n_s = 1$ for full filling. In order to hinge, symmetric systems need to be able to contract/expand [see Fig. 3.7(a)], which is not possible at fixed d. Indeed, Fig. 3.16(b) demonstrates that the number of excess zero modes starts growing from $\langle \Delta \rangle = 0$, rather than $\langle \Delta \rangle = 1$, as in Fig. 3.10(c). Furthermore, Fig. 3.16(b) shows that $\langle \Delta \rangle$ is maximum when the number of removed quads is $N_r = 10$. Denoting this maximum by $N_r^\star$, our goal is to determine Δ for all possible unit cell geometries at $N_r = N_r^\star$.

The number of possible unit cell geometries at $N_r = N_r^\star$ can be reduced by the consistent removal of the upper left quad (or any other quad) in

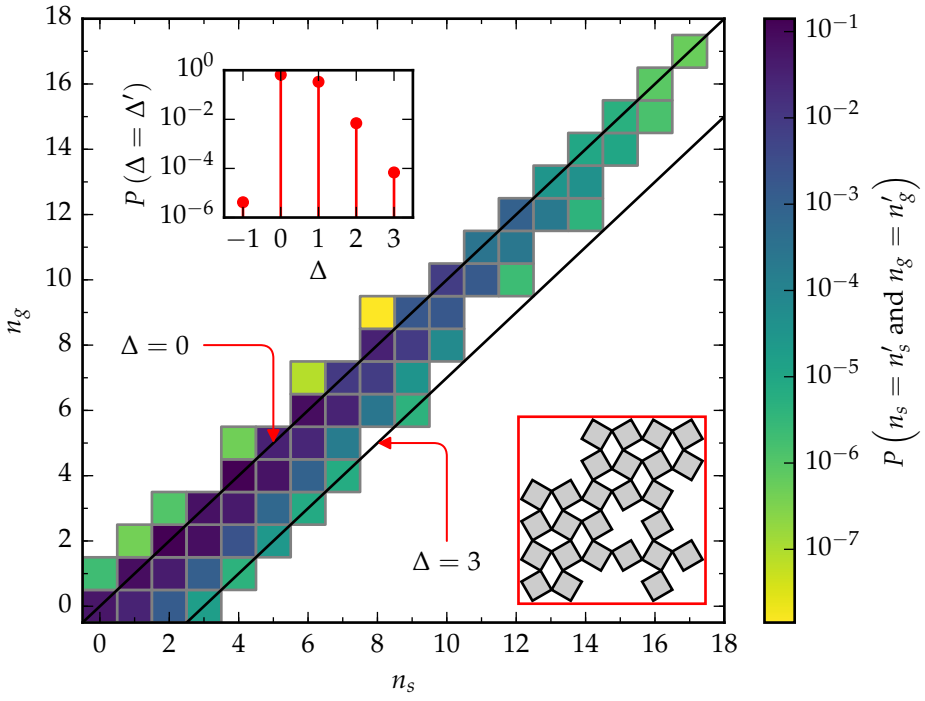

Figure 3.17: Discrete joint probability distribution as a function of n_s and n_g. The data comprises all possible geometries in a 6×6 periodic unit cell when 10 quads are removed. The black lines have constant Δ and its value is indicated by the arrows. Inset graph: Discrete probability distribution of Δ for the same data. Inset dilution geometry: An unit cell featuring $\Delta = 3$, for periodic boundaries.

each geometry we consider. Without loss of generality, this breaks the symmetry that comes with periodic boundaries. This leaves us with a total of

$$\binom{N_u^2 - 1}{N_r^\star - 1} = \binom{35}{9} \approx 7.1 \times 10^7 \tag{3.14}$$

geometries to consider, which takes approximately 4 days for our Python based code. For each geometry we have tracked n_s and n_g and their outcome is graphically displayed by a joint probability distribution in Fig. 3.17. For discrete variables this is also known as a joint probability mass function. In Fig. 3.17 black lines of slope unity represent contours

of constant Δ, with the main diagonal equivalent to $\Delta = 0$. We thus find that a periodic 6×6 system comprises maximally 3 excess zero modes, whereas the probability mass function of Δ (inset graph of Fig. 3.17) exposes that the appearance of $\Delta = 3$ constitutes a fraction $\sim 10^{-4}$ of the design space—tantamount to $\sim 7.1 \times 10^3$ unique cutting geometries, of which the particular unit cell depicted at the right bottom of Fig. 3.17 will be used to tile larger systems in section 3.4.1. The remaining part of the design space is mostly occupied by $\Delta = 0$, since bins of high probability are mainly located along the major diagonal of the joint probability distribution.

Surprisingly, however, Fig. 3.17 reveals that Δ can also become smaller than zero, although its appearance is rare, $P(\Delta = -1) \approx 10^{-6}$. In these cases generic systems, rather than symmetric systems, attain an extra near-zero mode that arises due to a special, coincidental combination of random quad distortions — we have verified these modes disappear when a different random quad distortion is imposed to the same cutting geometry. In particular, we found that near-zero modes typically exhibit $\lambda \approx 10^{-12}$, which is a few orders of magnitude larger than true numerical zero modes (Fig 3.9). Here we note that near-zero modes span a small part of the design space; their detailed consideration lies outside the scope of this thesis.

3.4.1 Tiling the unit cell

We now periodically tile the $N_u \times N_u$ unit cell to built larger $nN_u \times nN_u$ systems $(n = 2,3,\dots)$ [see Fig. 3.18(a) for $n = 2$], and determine their number of excess zero modes accordingly. Importantly, note that we use open boundary conditions for the tiled systems.

In Fig. 3.18(b) we display the number of excess zero modes of the tiled systems with n, which shows that the tiled systems (open circles, solid line) exhibit a significantly larger number of excess zero modes as compared to randomly diluted, non-tiled systems of identical size (dashed blue). Here, the dashed blue line describes the asymptotic growth of the average number of zero modes according to βN^2, with associated density $\beta = 0.01$ (see section 3.3.2). As can furthermore be observed, Δ of the tiled systems grows proportionally to $(nN_u)^2$, implying these systems are characterized by a constant density of zero modes. In particular, we have determined $\Delta/(nN_u)^2 \approx 0.06$ — which exceeds the density of zero

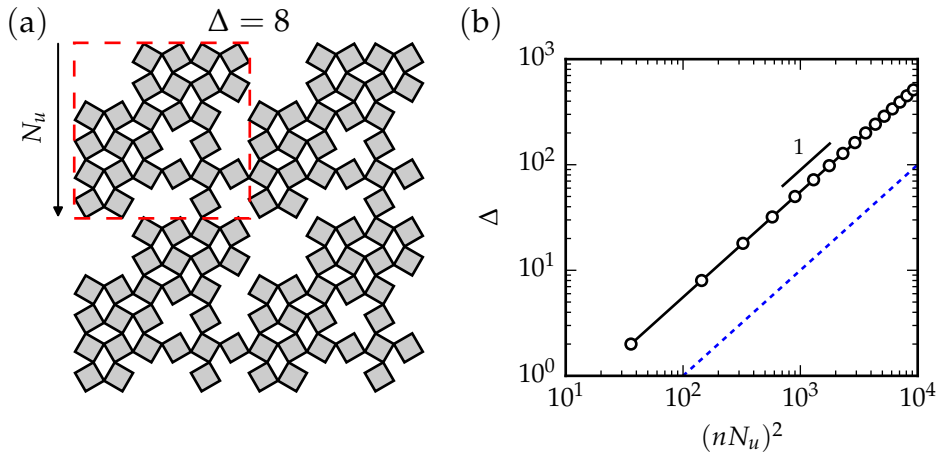

Figure 3.18: Excess modes in $nN_u \times nN_u$ systems built by the periodic tiling of a $N_u \times N_u$ unit cell ($n = 1,2,3,\dots$). (a) System corresponding to $n = 2$, resulting in $\Delta = 8$. The quads enclosed within the dashed red region display the unit cell. (b) The number of excess zero modes grows proportionally with $(nN_u)^2$ (open circles, solid line). We display data up to $n = 16$ ($nN_u = 96$). The blue dashed line represents the asymptotic growth of excess zero modes in randomly diluted systems as function of system size.

modes for random cutting by a factor 6. Hence, this procedure allows us to construct geometries for which Δ is 6 times larger as compared to the average maximum for random cutting ($\Delta/\Delta^\star \approx 6$), at a given system size.

3.5 Random bond removal

In this section we characterize the number of excess zero modes, Δ_b, for random bond removal, as function of the fraction of removed bonds, ρ_b, and system size N, and discuss differences and similarities with random quad removal.

In Fig. 3.19(a) we display $\langle \Delta_b \rangle (\rho_b, N)$ for system sizes $N = 10,20,\dots 80$, which are obtained using a similar procedure as devised for quad removal in section 3.3, now removing bonds rather than quads. Interestingly, these curves are qualitatively similar to results for quad removal (Fig. 3.12) and demonstrate that the number of excess zero modes may equally exceed one in systems where bonds are cut: Analogously to

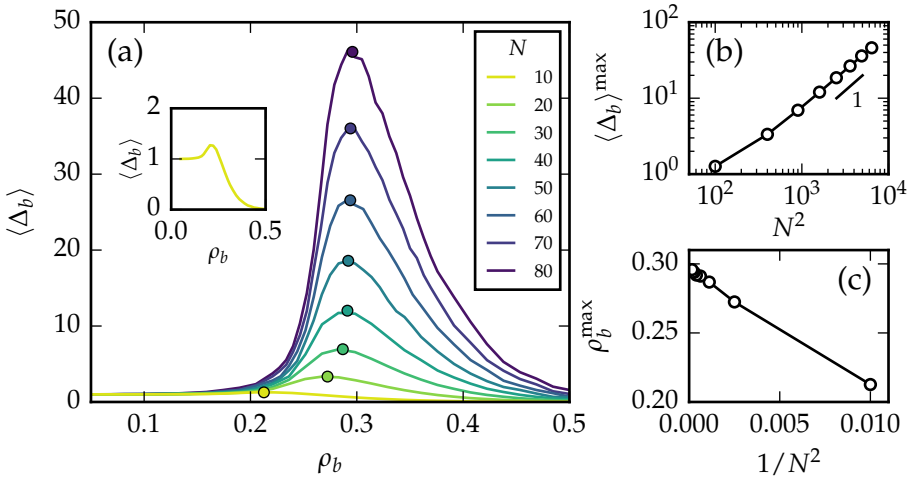

Figure 3.19: Statistics of the excess zero modes for random bond removal. (a) The average number of excess zero modes as function of the cutting fraction for a range of system sizes, using the same ensemble size as for random quad removal. Filled circles mark the maximum of each curve. Inset figure: Zoom in of $\langle\Delta_b\rangle(\rho_b)$ for $N = 10$. (b) The peak value grows linearly with N^2 for large N (log scale, slope 1), implying that $\langle\Delta_b\rangle^{\max} \sim N^2$. For small N, the scaling $\langle\Delta_b\rangle^{\max} \sim N^2$ exhibits finite size corrections proportional to $1/N^2$ (not shown). (c) The peak location tends to a constant as $1/N^2$.

quad removal, $\langle\Delta_b\rangle = 1$ for $\rho \approx 0$ and $\langle\Delta_b\rangle = 0$ for $\rho_b \to 0$ [see inset of Fig. 3.19(a)], whereas $\langle\Delta_b\rangle > 1$ for intermediate cutting fractions, albeit with an amplitude which is roughly 1.5 times smaller than for quad removal at given N. In the low cutting fraction limit ($\rho \approx 0$) systems are over-constrained and retain their rigidity in the generic case, even when some bonds are missing, leading to $\langle\Delta_b\rangle = 1$. In contrast, systems in the high cutting fraction limit ($\rho_b \to 1$) consist of many loosely connected quads that fail to constitute a rigid system in the generic case, hence $\langle\Delta_b\rangle = 0$.

To quantify differences and similarities between quad and bond removal, we follow section 3.3.2 and determine the peak value and location of $\langle\Delta_b\rangle$, which we denote $\rho_b^{\max}$ and $\langle\Delta_b\rangle^{\max}$, as function of the system size. The obtained results are shown in Fig. 3.19(b-c), and suggest the

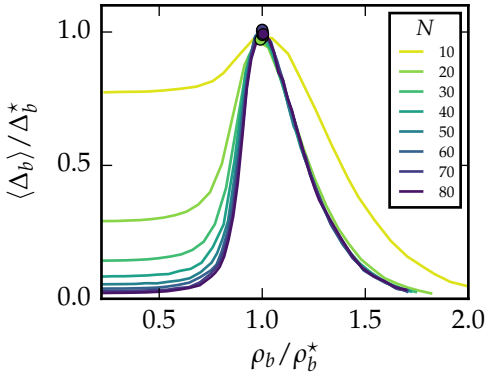

Figure 3.20: Scaling collapse for the $\langle\Delta_b\rangle$ curves in Fig. 3.19(a), obtained by rescaling the axes according to the relations given in Eqs. (3.15).

following asymptotic scaling relations:

$$\langle\Delta_b\rangle^{\max} \approx \langle\Delta_b\rangle^\star := \beta_b \left(1 + \frac{\alpha_b}{N^2}\right) N^2, \tag{3.15a}$$

and

$$\rho_b^{\max} \approx \rho_b^\star := \rho_{\infty,b} - \gamma_b / N^2, \tag{3.15b}$$

where $\alpha_b \approx 75$, $\beta_b \approx 0.007$, $\gamma_b \approx 8.37$ and $\rho_{\infty,b} \approx 0.3 \pm 0.01$ are constants with an interpretation similar to their analogues for quad removal in section 3.3. The asymptotic scaling relations and the values of their associated constants as obtained here reveal some contrasts between quad and bond removal.

First, similar to quad removal [Eq. (3.13a)], the peak value for bond removal grows proportionally to N^2, such that β_b can again be interpreted as the intrinsic spatial density of excess zero modes. Interestingly, we find that the intrinsic spatial density of zero modes for quad removal exceeds that of random bond removal by a factor $\beta/\beta_b \approx 1.5$, in agreement with the observation $\langle\Delta\rangle^{\max} > \langle\Delta_b\rangle^{\max}$. Apparently, the more correlated removal of bonds that occurs in quad removal (4 per removed quad) promotes the development of excess zero modes.

Second, the peak locations for bond and quad removal converge differently as function of N, but their peak locations in the $N \to \infty$ are the same within error bars: Whereas the peak location for quad removal

tends to the constant $\rho_\infty \approx 0.31 \pm 0.01$, the peak location for bond removal tends to the constant $\rho_{\infty,b} \approx 0.30 \pm 0.01$. We note that rescaling $\langle \Delta_b \rangle (\rho_b, N)$ according to Eqs. (3.15) yields a scaling collapse for large N (Fig. 3.20), demonstrating that $\langle \Delta_b \rangle$, similar to random quad removal, exhibits finite size scaling with simple mean field exponents.

In short, we have demonstrated that random bond removal qualitatively displays the same features as random quad removal. In both cases, the large N asymptotics prescribe that the peak tends to a constant location and that the number of excess zero modes grows proportionally to N^2. Quantitatively, we have found that the asymptotic peak peak location for quad and bond removal agrees within error bars, although the peak locations converge with different exponents. Furthermore, we have shown that the absolute number of excess zero modes is roughly 1.5 times larger for quad removal than for bond removal.

3.6 Conclusions

In this chapter we compared the number of zero modes in generic and symmetric collections of flexibly linked, rigid quads. We showed that symmetric systems featuring identical squares can possess excess zero modes that do not exist in generic systems consisting of irregular quads.

We have determined the average number of excess zero modes, $\langle \Delta \rangle$, for a large ensemble of independent, diluted systems, in which a fraction ρ of the total number of quads has been randomly removed. By using the same dilution pattern for symmetric and generic systems, we determined the ensemble averages $\langle \Delta \rangle (\rho, N)$ and revealed subtle but important differences between symmetric and generic systems. We found that $\langle \Delta \rangle \to 1$ for small cutting fractions ($\rho \to 0$), and $\langle \Delta \rangle \to 0$ for large cutting fractions ($\rho \to 1$). Interestingly, the number of excess zero modes at intermediate cutting fractions was shown to exhibit a maximum for which $\langle \Delta \rangle > 1$.

Subsequently, we determined $\langle \Delta \rangle (\rho, N)$ for a range of system sizes and showed that the peak value and location of $\langle \Delta \rangle$ exhibits simple scaling relations with N. By rescaling $\langle \Delta \rangle (\rho, N)$ using the relations for the peak value and location we obtained a scaling collapse, demonstrating that the average number of excess zero modes is an intrinsic quantity which exhibits finite size scaling with mean field exponents. By periodically tiling a 6×6 unit cell — with the maximum number of 3 excess

modes for periodic boundaries — we have also been able to design dilution geometries with a density of zero modes that is six times higher than the average for random cutting, independently of system size. Finally, for random bond removal, we have a found a very similar scaling collapse and peak location, with a density of zero modes that is roughly 1.5 times smaller than for random quad removal.

Appendix

3.A Constructing the gradient

The goal of this appendix is to analytically construct the energy gradient $\nabla E(\mathbf{X}) = \partial E/\partial \mathbf{X}$, which we will do by expressing the components of the gradient exclusively as functions of the corner coordinates of the quads. This procedure circumvents the need to determine derivatives using finite differences and leads to a significantly faster and more precise calculation of the gradient.

To calculate the gradient we use the energy as given in Eq. (3.6), which yields that

$$\frac{\partial E}{\partial \mathbf{X}} = \frac{1}{2}\frac{\partial}{\partial \mathbf{X}}\left(\sum_{s=0}^{N_b} \ell_s(\mathbf{X})^2\right). \tag{3.16}$$

Here $\ell_s(\mathbf{X})$ is some complicated function that describes the spring lengths as function of $\mathbf{X}$. Since springs are connected the corners of quads, we can express their square length as

$$\ell_s^2(\mathbf{X}) = \left[x_{n,i}(\mathbf{X}) - x_{m,j}(\mathbf{X})\right]^2 + \left[y_{n,i}(\mathbf{X}) - y_{m,j}(\mathbf{X})\right]^2, \tag{3.17}$$

where $(x_{n,i}, y_{n,i})$ and $(x_{m,j}, y_{m,j})$ describe the positions of the corners $(i = 0,1,2,3)$ of quad n and the corners $(j = 0,1,2,3)$ of quad m respectively. Following section 3.2, these corners can be calculated according to

$$\begin{pmatrix} x_{n,i} \\ y_{n,i} \end{pmatrix} = \begin{pmatrix} x_n \\ y_n \end{pmatrix} + \|\mathbf{e_{n,i}}\| \begin{pmatrix} \cos(\theta_{n,i} + \varphi_n) \\ \sin(\theta_{n,i} + \varphi_n) \end{pmatrix}, \tag{3.18}$$

with $\theta_{n,i} = \arg(\mathbf{e_{n,i}})$ the centre-to-corners angles of the quad, and where Eq. (3.18) similarly applies to quad m. Using the above relations, we now express the gradient components $\partial E/\partial x_n$, $\partial E/\partial y_n$ and $\partial E/\partial \varphi_n$ in terms of the corner coordinates $x_{n,i}$ and $y_{n,i}$. Note that we do not evaluate the obtained derivatives as function of the corner coordinates; although these can analytically calculated using Eq. (3.17), this would require specific knowledge about the dilution pattern as entitled in the adjacency matrix.

Derivatives with respect to x_n

Any change in the quad's coordinate x_n involves the x-displacement of the four corners. Therefore, the associated energy change is

$$\begin{aligned}\frac{\partial E}{\partial x_n} &= \frac{\partial E}{\partial x_{n,1}}\frac{\partial x_{n,1}}{\partial x_n} + \frac{\partial E}{\partial x_{n,2}}\frac{\partial x_{n,2}}{\partial x_n} + \frac{\partial E}{\partial x_{n,3}}\frac{\partial x_{n,3}}{\partial x_n} + \frac{\partial E}{\partial x_{n,4}}\frac{\partial x_{n,4}}{\partial x_n} \\ &= \sum_{i=1}^{4} \frac{\partial E}{\partial x_{n,i}}\frac{\partial x_{n,i}}{\partial x_n} \\ &= \sum_{i=1}^{4} \frac{\partial E}{\partial x_{n,i}},\end{aligned} \tag{3.19}$$

where we have used that $\partial x_{n,i}/\partial x_n = 1$, by Eq. (3.18).

Derivatives with respect to y_n

Similarly, the derivative of the energy with respect to y_n can be written as

$$\begin{aligned}\frac{\partial E}{\partial y_n} &= \sum_{i=1}^{4} \frac{\partial E}{\partial y_{n,i}}\frac{\partial y_{n,i}}{\partial y_n} \\ &= \sum_{i=1}^{4} \frac{\partial E}{\partial y_{n,i}}.\end{aligned} \tag{3.20}$$

Derivatives with respect to φ_n

Last, any change in the rotational angle φ_n introduces changes in both the x and y corner coordinates of quad n, yielding the following derivative for φ_n

$$\begin{aligned}\frac{\partial E}{\partial \varphi_n} &= \sum_{i=1}^{4} \left[\frac{\partial E}{\partial x_{n,i}}\frac{\partial x_{n,i}}{\partial \varphi_n} + \frac{\partial E}{\partial y_{n,i}}\frac{\partial y_{n,i}}{\partial \varphi_n} \right] \\ &= \sum_{i=1}^{4} \left[\|\mathbf{e_{n,i}}\| \left(\cos(\theta_i + \varphi_n) \frac{\partial E}{\partial y_{n,i}} - \sin(\theta_i + \varphi_n) \frac{\partial E}{\partial x_{n,i}} \right) \right],\end{aligned} \tag{3.21}$$

where we have substituted $\partial x_{n,i}/\partial \varphi_n = -\|\mathbf{e_{n,i}}\| \sin(\theta_i + \varphi_n)$ and $\partial y_{n,i}/\partial \varphi_n = \|\mathbf{e_{n,i}}\| \cos(\theta_i + \varphi_n)$, as obtained from Eq. (3.18).

3.B Constructing the Hessian matrix

Following the approach of appendix 3.A we now analytically determine the Hessian by expressing all second order derivatives of the energy in terms of the quads' corner coordinates. We therefore consider all possible second order partial derivatives of the energy with respect to the degrees of freedom of quad m and n, respectively given by (x_n, y_n, φ_n) and (x_m, y_m, φ_m). Below we determine the derivatives for the cases $m = n$ and $m \neq n$, which comprise a total of 12 independent types of partial derivatives.

Second derivatives with respect to x_m and x_n

$$\begin{aligned} \frac{\partial}{\partial x_m}\left(\frac{\partial E}{\partial x_n}\right) &= \frac{\partial}{\partial x_m}\sum_{i=1}^{4}\frac{\partial E}{\partial x_{n,i}} \\ &= \sum_{i=1}^{4}\frac{\partial}{\partial x_{n,i}}\frac{\partial E}{\partial x_m} \\ &= \sum_{i=1}^{4}\left[\frac{\partial}{\partial x_{n,i}}\sum_{j=1}^{4}\frac{\partial E}{\partial x_{m,j}}\right] \end{aligned} \tag{3.22}$$

For $m = n$, this yields:

$$\frac{\partial^2 E}{\partial x_n^2} = \sum_{i=1}^{4}\frac{\partial^2 E}{\partial x_{n,i}^2}, \tag{3.23}$$

For $m \neq n$ and under the assumption that corner i of quad n is connected to corner j of quad m, we obtain:

$$\frac{\partial^2 E}{\partial x_n \partial x_m} = \frac{\partial^2 E}{\partial x_{n,i}\partial x_{m,j}}, \tag{3.24}$$

Second derivatives with respect to y_m and y_n.

Following the approach to calculate the second derivatives with respect to x, we obtain

$$\frac{\partial^2 E}{\partial y_n^2} = \sum_{i=1}^{4}\frac{\partial^2 E}{\partial y_{n,i}^2}, \tag{3.25}$$

Under the assumption that corner i of quad n is connected to corner j of quad m, we obtain:

$$\frac{\partial^2 E}{\partial y_n \partial y_m} = \frac{\partial^2 E}{\partial y_{n,i} \partial y_{m,j}}. \tag{3.26}$$

Second derivatives with respect to φ_m and φ_n.

$$\frac{\partial}{\partial \varphi_m}\left(\frac{\partial E}{\partial \varphi_n}\right) = \frac{\partial}{\partial \varphi_m}\sum_{i=1}^{4}\left[\frac{\partial E}{\partial x_{n,i}}\frac{\partial x_{n,i}}{\partial \varphi_n} + \frac{\partial E}{\partial y_{n,i}}\frac{\partial y_{i,n}}{\partial \varphi_n}\right] \tag{3.27}$$

On the right hand side of the above equation, the first term within the summation represents the x contribution and the second term the y contribution for the derivative of E with respect to φ_n. For clarity we will first calculate the above derivative leaving out the second term, because the results for the first and second term will take an identical functional form. Therefore, we start with:

$$\begin{aligned}
&\frac{\partial}{\partial \varphi_m}\sum_{i=1}^{4}\frac{\partial E}{\partial x_{n,i}}\frac{\partial x_{n,i}}{\partial \varphi_n} \\
&= \sum_{i=1}^{4}\left[\frac{\partial^2 E}{\partial \varphi_m \partial x_{n,i}}\frac{\partial x_{n,i}}{\partial \varphi_n} + \frac{\partial E}{\partial x_{n,i}}\frac{\partial^2 x_{n,i}}{\partial \varphi_m \partial \varphi_n}\right] \\
&= \sum_{i=1}^{4}\left[\frac{\partial}{\partial x_{n,i}}\left(\sum_{j=1}^{4}\left[\frac{\partial E}{\partial x_{m,j}}\frac{\partial x_{m,j}}{\partial \varphi_m} + \frac{\partial E}{\partial y_{m,j}}\frac{\partial y_{m,j}}{\partial \varphi_m}\right]\right)\frac{\partial x_{n,i}}{\partial \varphi_n} + \frac{\partial E}{\partial x_{n,i}}\frac{\partial^2 x_{n,i}}{\partial \varphi_m \partial \varphi_n}\right] \\
&= \sum_{i=1}^{4}\left[\sum_{j=1}^{4}\left[\frac{\partial^2 E}{\partial x_{n,i}\partial x_{m,j}}\frac{\partial x_{m,j}}{\partial \varphi_m}\right]\frac{\partial x_{n,i}}{\partial \varphi_n} + \frac{\partial E}{\partial x_{n,i}}\frac{\partial^2 x_{n,i}}{\partial \varphi_m \partial \varphi_n}\right].
\end{aligned} \tag{3.28}$$

For $m = n$, this yields

$$\frac{\partial}{\partial \varphi_m}\sum_{i=1}^{4}\frac{\partial E}{\partial x_{n,i}}\frac{\partial x_{n,i}}{\partial \varphi_n} = \sum_{i=1}^{4}\left[\frac{\partial^2 E}{\partial x_{n,i}^2}\frac{\partial^2 x_{n,i}}{\partial \varphi_n^2} + \frac{\partial E}{\partial x_{n,i}}\frac{\partial^2 x_{n,i}}{\partial \varphi_n^2}\right]. \tag{3.29}$$

For $m \neq n$, and assuming that corner i of quad n is connected to corner j of quad m, we obtain from Eq. (3.28):

$$\frac{\partial}{\partial \varphi_m}\sum_{i=1}^{4}\frac{\partial E}{\partial x_{n,i}}\frac{\partial x_{n,i}}{\partial \varphi_n} = \frac{\partial^2 E}{\partial x_{n,i}\partial x_{m,j}}\frac{\partial x_{m,j}}{\partial \varphi_m}\frac{\partial x_{n,i}}{\partial \varphi_n}. \tag{3.30}$$

We have now calculated the outcome of Eq. (3.27) taking into account the x-contribution only. Because the y-contribution takes the same form as Eqs. (3.29-3.30), we obtain $(m = n)$:

$$\frac{\partial^2 E}{\partial \varphi_n^2} = \sum_{i=1}^{4} \left[\frac{\partial^2 E}{\partial x_{n,i}^2} \frac{\partial^2 x_{n,i}}{\partial \varphi_n^2} + \frac{\partial E}{\partial x_{n,i}} \frac{\partial^2 x_{n,i}}{\partial \varphi_n^2} + \frac{\partial^2 E}{\partial y_{n,i}^2} \frac{\partial^2 y_{n,i}}{\partial \varphi_n^2} + \frac{\partial E}{\partial y_{n,i}} \frac{\partial^2 y_{n,i}}{\partial \varphi_n^2} \right] \tag{3.31}$$

where $\partial^2 x_{n,i}/\partial \varphi_n^2 = -\|\mathbf{e_{n,i}}\| \cos(\theta_i + \varphi_n)$ and $\partial^2 y_{n,i}/\partial \varphi_n^2 = -\|\mathbf{e_{n,i}}\| \sin(\theta_i + \varphi_n)$, by Eq. (3.18). For $m \neq n$ we obtain:

$$\frac{\partial^2 E}{\partial \varphi_m \partial \varphi_n} = \frac{\partial^2 E}{\partial x_{n,i} \partial x_{m,j}} \frac{\partial x_{m,j}}{\partial \varphi_m} \frac{\partial x_{n,i}}{\partial \varphi_n} + \frac{\partial^2 E}{\partial y_{n,i} \partial y_{m,j}} \frac{\partial y_{m,j}}{\partial \varphi_m} \frac{\partial y_{n,i}}{\partial \varphi_n}. \tag{3.32}$$

Cross derivatives with respect to x_m, x_n, y_m and y_n.

$$\begin{aligned} \frac{\partial}{\partial y_m} \left(\frac{\partial E}{\partial x_n} \right) &= \frac{\partial}{\partial y_m} \sum_{i=1}^{4} \frac{\partial E}{\partial x_{n,i}} \\ &= 0, \end{aligned} \tag{3.33}$$

for both $m = n$ and $m \neq n$, because $\partial E/\partial x_{n,i}$ does not depend on y_m. Hence,

$$\frac{\partial^2 E}{\partial x_n^2} = 0, \tag{3.34}$$

and

$$\frac{\partial^2 E}{\partial x_m \partial x_n} = 0. \tag{3.35}$$

Cross derivatives with respect to x_m, x_n, φ_m and φ_n.

$$\begin{aligned}\frac{\partial}{\partial x_m}\left(\frac{\partial E}{\partial \varphi_n}\right) &= \frac{\partial}{\partial x_m}\sum_{i=1}^{4}\left[\frac{\partial E}{\partial x_{n,i}}\frac{\partial x_{n,i}}{\partial \varphi_n}+\frac{\partial E}{\partial y_{n,i}}\frac{\partial y_{i,n}}{\partial \varphi_n}\right]\\ &= \sum_{i=1}^{4}\left[\frac{\partial^2 E}{\partial x_m \partial x_{n,i}}\frac{\partial x_{n,i}}{\partial \varphi_n}+\frac{\partial E}{\partial x_{n,i}}\frac{\partial x_{n,i}^2}{\partial x_m \varphi_n}\right]\\ &= \sum_{i=1}^{4}\left[\frac{\partial}{\partial x_{n,i}}\left(\sum_{j=1}^{4}\frac{\partial E}{\partial x_{m,j}}\right)\frac{\partial x_{n,i}}{\partial \varphi_n}\right]\\ &= \sum_{i=1}^{4}\left[\sum_{j=1}^{4}\left[\frac{\partial^2 E}{\partial x_{n,i}\partial x_{m,j}}\right]\frac{\partial x_{n,i}}{\partial \varphi_n}\right].\end{aligned} \tag{3.36}$$

For $m = n$, this yields

$$\frac{\partial^2 E}{\partial x_n \partial \varphi_n} = \sum_{i=1}^{4}\frac{\partial^2 E}{\partial x_{n,i}^2}\frac{\partial x_{n,i}}{\partial \varphi_n}. \tag{3.37}$$

And for $m \neq n$, assuming that corner i of quad m is connected to corner j of quad n, we obtain

$$\frac{\partial^2 E}{\partial x_m \partial \varphi_n} = \frac{\partial^2 E}{\partial x_{n,i}\partial x_{m,j}}\frac{\partial x_{n,i}}{\partial \varphi_n}. \tag{3.38}$$

Cross derivatives with respect to y_m, y_n, φ_m and φ_n.

The derivation is identical to the cross derivatives with respect to x and φ. For $m = n$, the result therefore is

$$\frac{\partial^2 E}{\partial y_n \partial \varphi_n} = \sum_{i=1}^{4}\frac{\partial^2 E}{\partial y_{n,i}^2}\frac{\partial y_{n,i}}{\partial \varphi_n}. \tag{3.39}$$

And for $m \neq n$, assuming that corner i of quad m is connected to corner j of quad n, we obtain

$$\frac{\partial^2 E}{\partial y_m \partial \varphi_n} = \frac{\partial^2 E}{\partial y_{n,i}\partial y_{m,j}}\frac{\partial y_{n,i}}{\partial \varphi_n}. \tag{3.40}$$